International Symposium
On Turbulence and Shear Flow
Phenomena (TSFP-8)
August 28 - 30, 2013 Poitiers, France

LARGE-EDDY SIMULATION OF PASSIVE SHOCK-WAVE/BOUNDARY-LAYER INTERACTION CONTROL

Vito Pasquariello, Jan Matheis, Muzio Grilli and Stefan Hickel
Institute of Aerodynamics and Fluid Mechanics
Technische Universität München
Boltzmannstr. 15, D-85748 Garching
vito.pasquariello@tum.de

ABSTRACT

We investigate a passive flow-control technique for the interaction of an oblique shock generated by an 8.8° wedge with a turbulent boundary layer at a free-stream Mach number of $M_\infty = 2.3$ by means of large-eddy simulation. The control configuration studied combines suction applied inside the separation zone and injection acting upstream of the interaction region through a passive-channel concept. We present results for three configurations, which differ in the suction location within the recirculation zone while the injection position is kept constant. Besides the analysis of mean flow properties, the main focus lies on the turbulence evolution within the interaction region and the effect of the control devices on the low-frequency dynamics of the reflected shock movement.

INTRODUCTION

Shock-wave/boundary-layer interactions (SWBLI) frequently occur in flows of technological interest, such as supersonic air intakes, turbomachine cascades, helicopter blades, supersonic nozzles and launch vehicles in general. SWBLI can critically affect the vehicle or machine performance in several ways. The adverse pressure gradient acting on the flow strongly retards the boundary layer, eventually leading to separation if the imposed pressure gradient is strong enough (Délery & Dussauge, 2009). Furthermore, the SWBLI is a main cause of maximum mean and fluctuating pressure levels as well as thermal loads that a structure is exposed to. The low-frequency unsteadiness of the reflected shock, whose exact mechanism is still under debate, is a main contribution to failure due to fatigue (Pirozzoli *et al.*, 2010).

Several experiments and numerical investigations have been carried out with the aim of identifying suitable control mechanisms that mitigate or preferably eliminate the detrimental effects caused by shock-induced separation, see Délery (1985). In this work we focus on a control technique that consists of a combination of suction applied inside the separation bubble and injection acting ahead of the interaction region, see Fig. 1. Both suction and injection are realized through a passive channel and act over the whole spanwise domain extent, which leads to a quasi two-dimensional flow pattern.

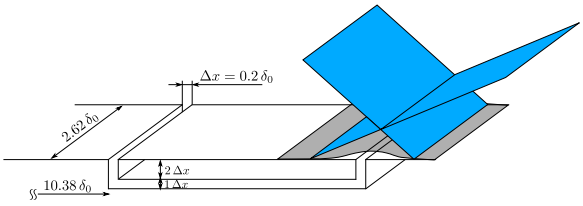

Figure 1: Schematic of the considered control method. Blue planes: reflected shock system. Grey Surface: 2D sketch of the recirculation region.

FLOW CONFIGURATION AND NUMERICAL APPROACH

The basic SWBLI topology studied in this work is the case of an oblique shock impinging on a flat plate boundary layer. The resulting flow pattern is shown in Fig. 2. The shock is generated by a 8.8° wedge at a freestream Mach number of $M_\infty = 2.3$ and the Reynolds number based on the inlet boundary layer thickness is $\mathrm{Re}_{\delta_0} = 60.5 \cdot 10^3$. Stagnation temperature and pressure are $T_0 = 300\,\mathrm{K}$ and $p_0 = 0.5\,\mathrm{bar}$. Throughout this study we will use the boundary layer thickness either evaluated at the domain inlet $\delta_0 = 11.35\,\mathrm{mm}$ or at a reference plane $\delta_0^r = 13.46\,\mathrm{mm}$ located upstream of the interaction region at $x/\delta_0 = 11.7$ as reference length.

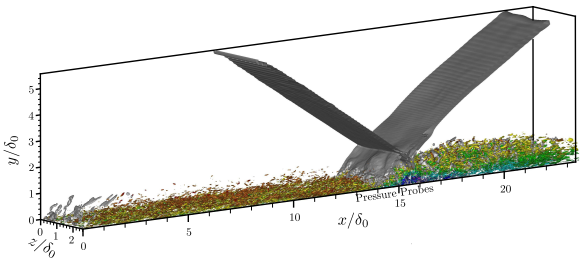

Figure 2: Illustration of the computational domain together with isocontours of pressure gradient magnitude (gray) and Q-criterion, colored by local streamwise velocity.

At the domain inlet a Digital Filter (DF) based boundary condition is used (Touber & Sandham, 2009), for which first and second order statistical moments have been obtained through a precursor temporal boundary layer simulation. The shock is introduced at the top of the domain, by imposing a jump in the flow variables that satisfies the Rankine-Hugoniot relations. The nominal inviscid im-

pingement point at the wall is $x_{imp} = 16.7\,\delta_0$. At the outlet, linear extrapolation of all flow variables is used. The wall is modeled as isothermal with the temperature set fixed to its nominal adiabatic value $T_w/T_\infty = 1 + r\frac{\gamma-1}{2}M_\infty^2 = 2.065$, which corresponds to a recovery factor of $r = 1$. Periodic boundary conditions are used in the spanwise direction. The domain is rectangular with dimensions $23.39\delta_0 \times 5.57\delta_0 \times 2.62\delta_0$ and is discretized with $560 \times 190 \times 130$ cells in streamwise, wall-normal and spanwise directions, respectively. This leads to a grid resolution of $\triangle x^+ = 30$, $\triangle y^+_{min} = 1.2$, $\triangle z^+ = 15$. For the low-frequency analysis presented later, 10387 equally spaced pressure probes ($\triangle/\delta_0^r \approx 0.05$) have been placed both in stream- and spanwise direction along the wall as indicated in Fig. 2.

Fig. 1 shows a schematic representation of the basic control method used in this work together with the main geometry parameters. In total three parameter sets have been investigated, for which the suction location within the separated zone is varied while the injection position is kept fix. Intuitively, vertical injection perturbs the incoming turbulent boundary layer, followed by a relaxation process before the interaction region is reached. For this reason the injection is located well upstream of the nominal inviscid impingement point. Fig. 3 shows the average normalized wall-pressure distribution for the baseline configuration without control, referred to as NC in the following, together with the bubble topology represented through the $<u>/U_\infty = 0$ iso-line (•). Grey shaded rectangles represent three different suction locations. With CA we denote the case where suction is applied near the maximum bubble height and for the cases CB and CC the suction slot is shifted $0.3\,\delta_0$ upstream and downstream, respectively.

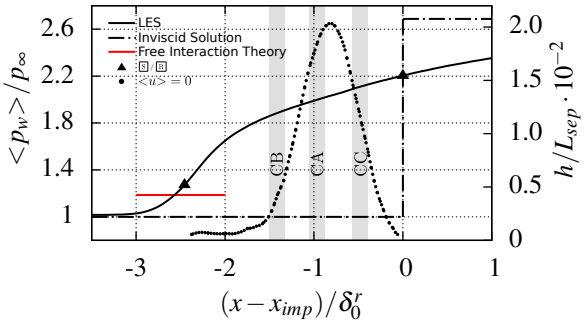

Figure 3: Average normalized wall-pressure distribution and zero streamwise velocity iso-line for the uncontrolled reference configuration NC. Investigated suction locations are indicated by CA, CB and CC. Triangles (▲) denote separation and reattachment pressure levels, respectively

Implicit Large-Eddy Simulations (ILES) are conducted for the aforementioned flow configurations. The compressible Navier-Stokes equations are solved using the Adaptive Local Deconvolution Method (ALDM) for the discretization of the convective fluxes (Hickel & Larsson, 2009). The diffusive fluxes are discretized using a 2^{nd} order central difference scheme and a 3^{rd} order Runge Kutta scheme is used for the time integration.

Reported statistical quantities have been obtained by averaging instantaneous three-dimensional flow fields in time and spanwise direction after an initial transient of $5\,L_x/U_\infty$; see Tab. 1 for details.

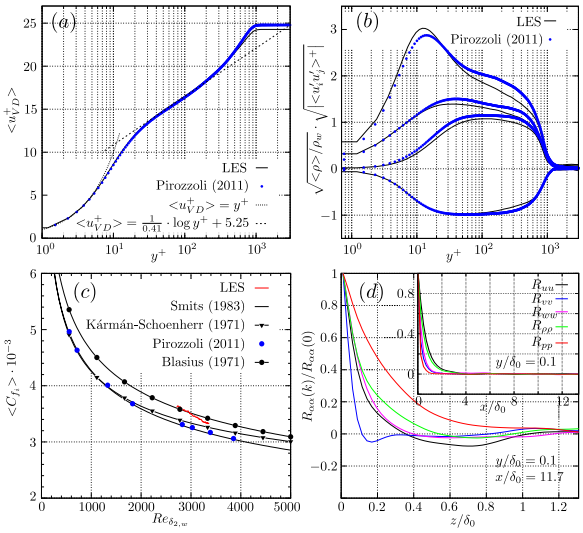

Figure 4: Incoming boundary layer: (a) van-Driest transformed mean-velocity profile. (b) RMS of Reynolds stresses with density scaling at $Re_\tau = 900$. (c) Incompressible skin friction evolution (d) Two-point autocorrelation functions.

RESULTS AND DISCUSSION

Incoming Turbulent Boundary Layer

Before the influence of each control configuration on the SWBLI is addressed, the main incoming boundary layer properties will be discussed. The van-Driest transformed mean-velocity profile together with the RMS of Reynolds stresses in Morkovin scaling at $x/\delta_0 = 13.1$ are presented in Fig. 4 (a)/(b) and compared against DNS data of Pirozzoli & Bernardini (2011) for a slightly different Mach number of $M_\infty = 2.0$ but the same friction Reynolds number $Re_\tau = 900$. The velocity profile is in excellent agreement with the logarithmic law of the wall and the DNS data. For the Reynolds stresses good agreement can be observed in the near-wall region, while larger deviations occur in the logarithmic and wake region. For further validation, the incompressible skin friction distribution $<C_{f_i}>$, obtained through the van-Driest II transformation, is compared to algebraic incompressible relations and the same DNS database; see Fig. 4 (c). The computed incompressible skin friction coefficient (—) is in good agreement with the reported empirical relations. Autocorrelation functions in spanwise direction, see Fig. 4 (d), show that all flow variables are sufficiently decorrelated over a distance equal to half of the spanwise domain extent. From this we conclude that the domain is sufficiently wide and that the turbulence dynamics is not affected by the periodic boundary conditions. In the same figure, also the streamwise evolution of the autocorrelation functions is illustrated. It is important to note, that the DF technique does not introduce any spurious low-frequency tone which could possibly interfere with the reflected shock dynamics investigated in this study.

Baseline SWBLI

The mean skin-friction evolution in the direct vicinity of the interaction region is shown in Fig. 5. Due to the adverse pressure gradient imposed on the turbulent boundary layer, the flow is decelerated and forms a recirculation zone as indicated by the change of sign in $<C_f>$. The mean separation length for the baseline configuration is $L_{sep} = 2.46\,\delta_0^r$. The corresponding wall-pressure evo-

lution is shown in Fig. 3. The pressure increase associated with the impinging shock is felt approximately $3\,\delta_0^r$ before the theoretical inviscid impingement location x_{imp}. This effect is known as the upstream influence mechanism (Délery, 1985). Black triangles denote the separation and reattachment pressure levels, while the horizontal red line marks the separation pressure as predicted by the free-interaction theory. The bubble topology, analyzed through the $<u>/U_\infty = 0$ iso-line in Fig. 3, reveals a very shallow separation zone with an aspect ratio of $h_{max}/L_{sep} = 50$. Dupont *et al.* (2006) proposed a linear relationship for weak interactions between the interaction length L_{int} and the pressure jump across the impinging shock wave $(p_2 - p_1)$ normalized by the upstream boundary layer thickness δ_0 and wall shear stress τ_w, respectively. In this study we define the distance between the mean reflected shock foot position (obtained through linear extrapolation to the wall) and x_{imp} as the interaction length L_{int}, as done by Dupont *et al.* (2006). Fig. 5 depicts the experimental data together with the value for the current LES •, confirming the expected linear relationship.

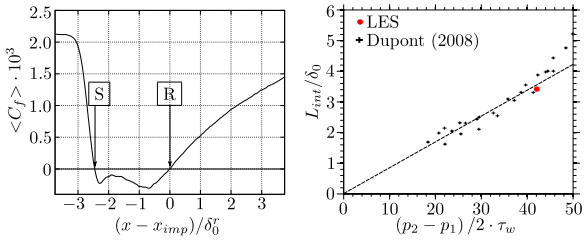

Figure 5: Mean-flow statistics: skin friction evolution and interaction length.

In the following we analyze the Power Spectral Densities (PSD) of wall-pressure probes. Pressure signals have been recorded at a mean sampling time interval of $0.051\,\delta_0^r/U_\infty$ and cover a total timespan of $1091\,\delta_0^r/U_\infty$; see Tab. 1 for details. This leads to a maximum resolvable Strouhal number of $St_{max} \approx 10$ and a minimum resolvable Strouhal number of $St_{min} \approx 0.001$, which means that the current LES is able to capture the expected low-frequency unsteadiness. In Fig. 6 we report the wall-pressure spectrum together with the full evolution of pressure fluctuations evaluated at four selected streamwise locations. Moreover, mean separation and reattachment positions are indicated. In order to emphasize the frequencies that contribute most, we show contours of the premultiplied PSD normalized by the integrated PSD over a given frequency range, i.e., $f \cdot \mathrm{PSD}(f)/\int \mathrm{PSD}(f)\mathrm{d}f$. This scaling explains why the high-frequency band near the reflected shock foot position seems to be discontinuous.

The most upstream wall-pressure variance signal shows no significant pressure variation, indicating the undisturbed turbulent boundary layer. Considering the next probe, which is located in the proximity of the mean reflected shock foot, distinctive pressure peaks associated with the back and forth motion of the reflected shock can be identified. Dussauge *et al.* (2006) found typical Strouhal numbers based on the separation length ranging between $St_{L_{sep}} = 0.02 \ldots 0.05$ for different flow geometries and upstream conditions. Associated time scales of $tU_\infty/L_{sep} = 20 \ldots 50$ could be found in the current LES as indicated in Fig. 6. Further downstream, distinct peaks are no longer visible, however, the amplitude of the pressure fluctuations has increased significantly as a consequence of turbulence

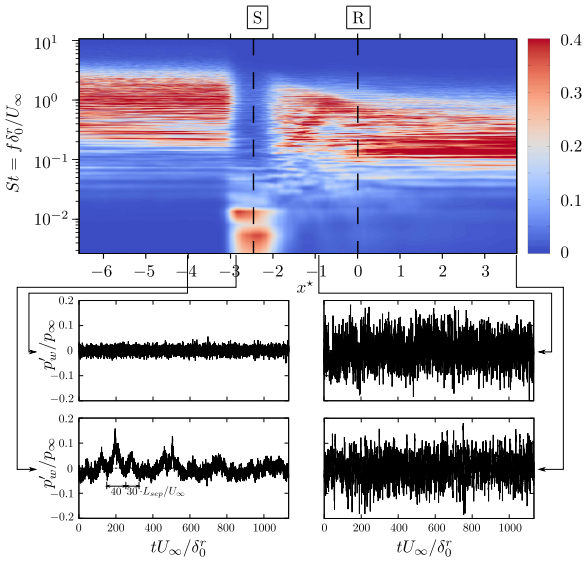

Figure 6: Weighted power spectral density (PSD) of spanwise-averaged wall-pressure probes for the baseline configuration and selected pressure signals. Contour: $f \cdot \mathrm{PSD}(f)/\int \mathrm{PSD}(f)\mathrm{d}f$, $x^\star = (x - x_{imp})/\delta_0^r$.

amplification over the shock. The PSD spectrum in Fig. 6 clearly shows the broadband peak associated with the characteristic frequency of the energetic scales in the undisturbed boundary layer. The energy peak shifts towards significantly lower frequencies in the vicinity of the mean separation location and moves back again to higher frequencies downstream of the interaction zone. Due to the thickening of the boundary layer past the shock system, the new PSD peak is located at lower Strouhal numbers. Based on the mean separation length a Strouhal number of $St_{L_{sep}} = fL_{sep}/U_\infty = 0.03$ is found for the low-frequency shock motion. This finding is consistent with the experimental values documented in Dupont *et al.* (2006). As reported in Tab. 1, a total number of 14 low-frequency cycles (LFC) are captured within the available integration time.

Table 1: Numerical details and results of all cases.

CASE	*NC*	*CA*	*CB*	*CC*
SETUP: STATISTICS				
Sampling time $\Delta t\,U_\infty/\delta_0^{r\,a}$	1.06	1.06	1.06	1.06
Sampling time $\Delta t\,U_\infty/\delta_0^{r\,b}$	0.051	0.029	0.029	0.029
Number of FTT	55	27	38	35
Runtime^c $T\,U_\infty/\delta_0^r$	1091	538	754	694
RESULTS: MEAN STATISTICS				
Interaction length^e L_{int}/δ_0^r	3.24	3.26	2.75	3.09
Massflow ratio $\dot{m}_{ch}/\dot{m}_{bl}$ [%]	–	2.66	2.05	3.15
Max. bubble height h_{max}/δ_0^r	0.035	0.081	0.036	0.068
Bubble mass^f $m/(\rho_\infty {\delta_0^r}^2)$	0.032	0.024	0.011	0.014
RESULTS: LF-ANALYSIS				
$St = f\delta_0^r/U_\infty{}^d$	0.0135	0.0238	0.0329	0.0242
Number of LFC	14	12	24	16

a. Sampling time for the post-processing based on collected snapshots *b*. Mean sampling interval for the wall-pressure probes *c*. Excluding a start-up transient of 5 FTT. *d*. See Fig. 11 for details. *e*. Distance between the mean reflected shock foot position and theoretical inviscid impingement point. *f*. Bubble mass per unit span.

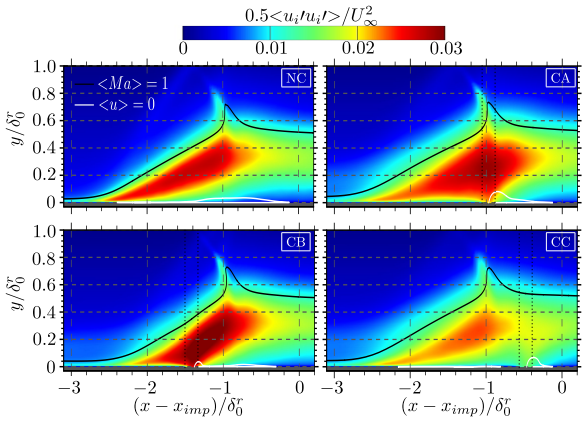

Figure 8: Mean resolved turbulent kinetic energy together with zero streamwise velocity iso-line in white and sonic line in black in the vicinity of the interaction zone. Vertical dotted lines represent suction locations.

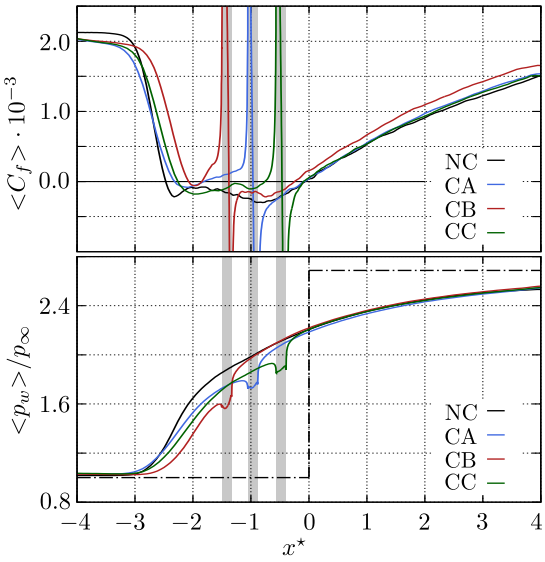

Figure 9: Skin friction and wall pressure distribution in the vicinity of the interaction region. Grey shaded areas indicate suction locations.

Control configurations

In this section, we provide a cross-comparison between the baseline configuration NC and the three control-mechanisms CA, CB and CC. The skin friction evolution in Fig. 9 shows a perturbation of the upstream boundary layer for all three control cases due to the vertical injection. Local suction within the separation bubble leads to an increase in skin friction directly upstream of the suction location due to the acceleration of the near-wall flow. Downstream of the suction slot, the skin friction level drops to greater negative values due to the higher reversed flow amplitude. All control configurations lead to a downstream shift of the mean separation location. The largest effect is observed for control case CB. For the same case, the skin friction evolution downstream of the suction channel is positively influenced as indicated by the upstream shift of the mean reattachment position and the overall higher skin friction level in the relaxation zone. The mean wall pressure distribution in Fig. 9 clearly shows a reduction of the upstream influence length for control case CB. The interaction lengths L_{int}/δ_0^r are 3.24, 3.26, 2.75 and 3.09 for the cases NC, CA, CB and CC, respectively.

A close-up of the interaction zone is shown in Fig. 8, where we present contours of mean turbulent kinetic energy (TKE), the zero streamwise velocity iso-line in white and the sonic line in black. Without flow control, turbulence gets amplified when approaching the shock system with maxima being located in the region around the mean separation location and along the detached shear layer that originates from it. For all control configurations, the incoming subsonic layer is thicker than for the baseline case. This is a direct consequence of the vertical injection upstream of the SWBLI. However, the zero streamwise velocity iso-line shows that control cases CA and CB are able to significantly reduce the spatial extent of the recirculation zone upstream of the suction slots. Geometric properties are summarized in Tab. 1. Considering the TKE contours, suction applied within the inclined detached shear layer region ($-2.6 < x^\star < -0.8$) leads to a strong amplification of turbulence, whereas if suction is applied in the rear part of the bubble (CC) it damps turbulent fluctuations. For all three control configurations an increased incoming turbulence level can be observed up to wall distances $y/\delta_0^r \approx 0.3$, which results from additional shear layers directly downstream of the injection slot, see Fig. 7. Compared to the undisturbed turbulent boundary layer, the maximum amplification factor within the interaction region is found to be 2.64 for NC, 2.82 for CA, 3.19 for CB and 2.29 for CC, again highlighting a lower turbulence amplification of normal stresses for control case CC compared to the baseline

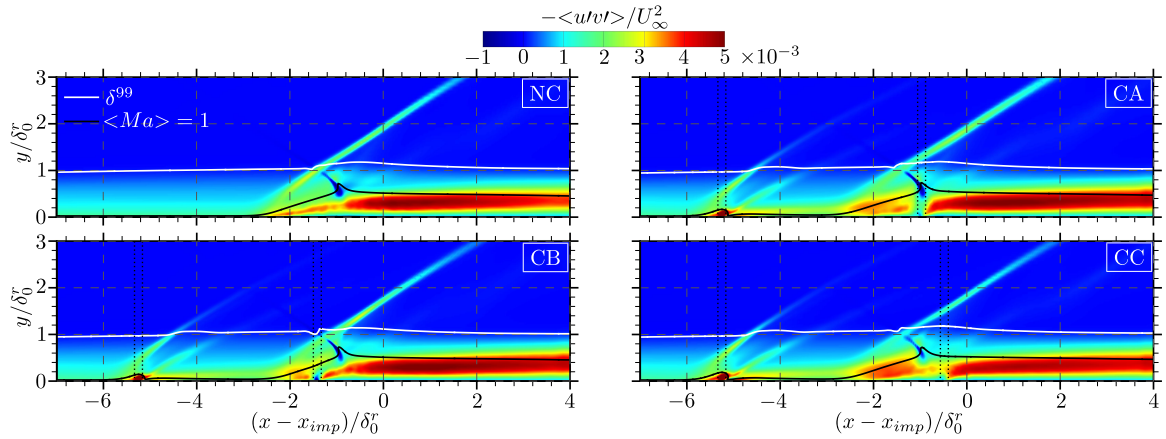

Figure 7: Mean resolved turbulent shear stress together with boundary layer thickness iso-line in white and sonic line in black. Vertical dotted lines represent suction and injection locations.

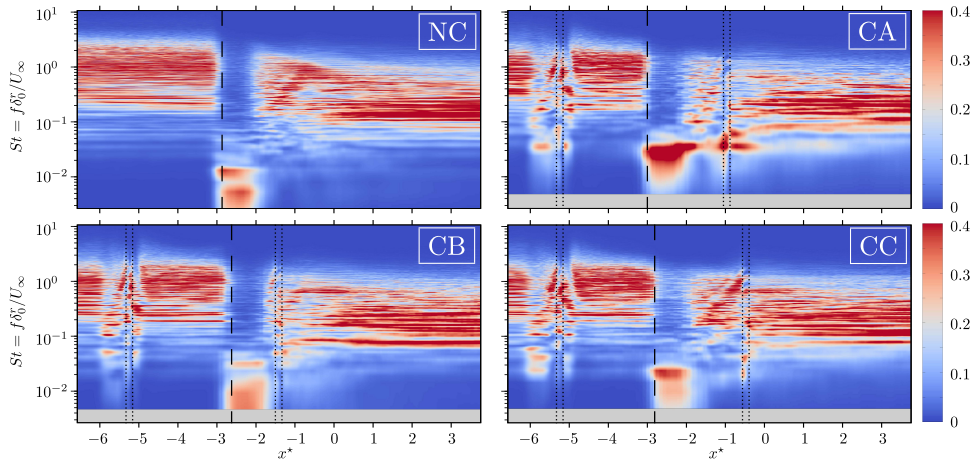

Figure 10: Weighted power spectral density (PSD) of spanwise-averaged wall-pressure probes for all cases studied. Contour: $f \cdot \mathrm{PSD}(f)/\int \mathrm{PSD}(f)\mathrm{d}f$, $x^\star = \left(x - x_{imp}\right)/\delta_0^r$.

configuration. By investigating contours of turbulence production $P = -\overline{\rho}\widetilde{u_i''u_j''}\frac{\partial \tilde{u}_i}{\partial x_j}$ (not shown here), we found that the deflection of the shear layer towards the suction location strongly excites turbulence production. This in turn explains the higher turbulent kinetic energy level for control cases CA and CB in this region. As it will be seen below, the reflected shock dynamics is significantly weakened for case CC, which possibly explains the overall lower turbulence amplification for this configuration.

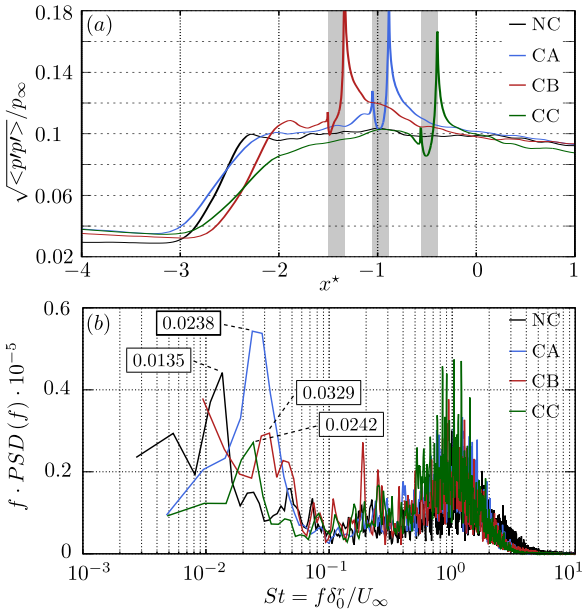

Figure 11: (a) Longitudinal evolution of wall-pressure fluctuations. (b) Weighted power spectral density for all cases studied. The spectra have been evaluated at the streamwise locations indicated in Fig. 10.

Fig. 7 shows the resolved mean turbulent shear stress, the boundary layer thickness evolution (white) and the sonic line (black) for all cases. For the baseline configuration a high level of shear stress is found along the detached shear layer within the interaction region $-3 < x^\star < 1$. Its maximum is located approximately one boundary layer thickness downstream of the mean reattachment location ($x^\star \approx 1$), confirming the findings by Pirozzoli & Grasso (2006). A high $<u'v'>$ level is found along the reflected shock, which is consistent with experimental measurements by Piponniau (2009) and directly associated with the unsteady shock motion. The turbulent shear stress changes its sign at the tip of the incident shock as a consequence of its flapping motion (Shahab, 2006). For all control cases additional unsteady shocks can be identified in the vicinity of the injection slots. At the same location, the formation of shear layers due to small recirculation zones directly upstream and downstream of the injection position leads to an increased level of turbulence in this region, which is then convected downstream and interacts with the original reflected shock. The adverse pressure gradient induced by the reflected shock bulges the incoming shear layer, resulting in a spot of increased shear stress within the interaction zone. This phenomenon is more pronounced for control cases CA and CC. It is interesting to note that the flapping motion of the incident shock tip and the reflected shock dynamics are significantly reduced for configuration CC.

Considering the overall boundary layer thickness evolution (white line in Fig. 7), one can conclude that the present control mechanism neither improves nor worsens the downstream boundary layer.

The influence of the suction location on unsteady aspects related to the reflected shock dynamics is investigated in the following. For this purpose, Fig. 10 illustrates the wall-pressure spectrum for all cases studied. As already observed in Fig. 7, all control configurations exhibit additional low-frequency contents near the injection and suction position. The broadband peak centered around $St \approx 1$ after the suction location indicates that none of the investigated control techniques alters the large-scale turbulence dynamics upstream of the interaction zone significantly. A low-frequency peak associated with the reflected shock dynamics is still apparent for all three cases but shifted to higher Strouhal numbers. One could argue that this is a direct consequence of the lower bubble mass (Souverein & Debiève, 2010). The acoustic coupling provided by the passive-channel concept explains the same level of low-frequency content present for the recirculation zones in the direct vicinity of the suction and injection positions as for the reflected shock. The characteristic Strouhal number associated with an acoustic disturbance that travels through the channel with the local speed of sound is $St \approx 0.15$, which is approximately one order of magnitude greater than the characteristic low-frequencies observed in Fig. 10. We can therefore exclude influences of an acoustic feedback

loop through the channel.

Distributions of $\sqrt{<p'p'>}/p_\infty$ within the interaction region are shown in Fig. 11 (a). Large amplifications of the pressure fluctuations are found around the reflected shock foot, while secondary peaks can be observed at the discrete suction locations. Besides the change in interaction length L_{int} as already discussed in conjunction with the wall-pressure evolution, Fig. 9, one can further observe a significantly lower amplification level for control configuration CC near the reflected shock foot and after the SWBLI, consistent with previous discussions related to Figs. 8 and 7. Fig. 11 (b) shows the weighted power spectral density for all cases evaluated at selected streamwise locations. The spectra $f \cdot \mathrm{PSD}(f)$ are plotted in a linear scale against $\log(f)$, resulting in an energetic scaling, since the area under the resulting curve becomes proportional to the energy $E^2_{f_a-f_b}$ of the signal lying between f_a and f_b (Gatski & Bonnet, 2009):

$$E^2_{f_a-f_b} = \int_{f_a}^{f_b} [f \cdot \mathrm{PSD}(f)]\, \mathrm{d}(\log f) \qquad (1)$$

The Strouhal numbers associated to the maximum energy of the signal in the low-frequency range are highlighted. We measure Strouhal numbers of 0.0135 for NC, 0.0238 for CA, 0.0329 for CB and 0.0242 for CC, thus $St_{NC} < St_{CA} < St_{CC} < St_{CB}$. The mean bubble mass per unit span, see Tab. 1, follows the trend $m_{NC} > m_{CA} > m_{CC} > m_{CB}$, supporting the theory of the pulsation of the recirculation zone being responsible for the low-frequency unsteadiness observed (Pirozzoli *et al.* (2010), Grilli *et al.* (2012)). The spectra further highlight an increase in energy for control case CA (see also Fig. 10) compared to the baseline configuration, while all other control cases lead to lower amplitudes.

CONCLUSION

We studied a passive flow-control mechanism for the interaction of an oblique shock with a turbulent flat-plate boundary layer. We found that suction applied within the separation zone significantly alters the turbulence evolution in this region. Suction acting within the range of the inclined detached shear layer (CA and CB) strongly amplifies turbulence through a deflection towards the discrete suction slot, whereas suction when applied in the rear part of the separation bubble (CC) lowers the overall turbulence level. Of course not only the shear layer contributes to turbulence amplification, but also the unsteady motion of the reflected shock. By investigating contours of resolved turbulent shear stress we found that control configuration CC significantly reduces the reflected shock dynamics and the flapping motion associated with the incident shock tip. Both findings support the observation of reduced turbulence amplification for this case compared to the baseline configuration without control (NC).

The influence of the control method on the low-frequency unsteadiness has been addressed through a Fourier analysis of wall-pressure probes. All configurations alter the high-energy low-frequency content associated with the reflected shock by shifting it to higher frequencies, possibly as a direct consequence of the reduction in bubble mass. The most upstream suction position (CB) is most efficient and leads to the lowest bubble mass. Weighted power spectral densities in energetic scaling reveal an increased low-frequency energy level for case CA and a lowered low-frequency energy level for the cases CB and CC. The streamwise evolution of wall pressure fluctuations $\sqrt{<p'p'>}/p_\infty$ shows a significant reduction of wall pressure loads for control case CC around the mean reflected shock foot, which is a direct consequence of the mitigated reflected shock dynamics.

REFERENCES

Délery, J. 1985 Shock wave/turbulent boundary layer interaction and its control. *Progress in Aerospace Sciences* **22** (4), 209–280.

Délery, J. & Dussauge, J.-P. 2009 Some physical aspects of shock wave/boundary layer interactions. *Shock Waves* **19** (6), 453–468.

Dupont, P., Haddad, C. & Debiève, J.-F. 2006 Space and time organization in a shock-induced separated boundary layer. *Journal of Fluid Mechanics* **559**, 255.

Dussauge, J.-P., Dupont, P. & Debiève, J.-F. 2006 Unsteadiness in shock wave boundary layer interactions with separation. *Aerospace Science and Technology* **10** (2), 85–91.

Gatski, T. B. & Bonnet, J.-P. 2009 *Compressibility, Turbulence and High Speed Flow*.

Grilli, M., Schmid, P. J., Hickel, S. & Adams, N. A. 2012 Analysis of unsteady behaviour in shockwave turbulent boundary layer interaction. *Journal of Fluid Mechanics* pp. 1–13.

Hickel, S. & Larsson, J. 2009 On implicit turbulence modeling for LES of compressible flows. In *Advances in Turbulence XII* (ed. B. Eckhardt), pp. 873–875. Springer Berlin Heidelberg.

Piponniau, S. 2009 Instaionnarités dans les décollements compressibles: cas des couches limites soumises à ondes de choc. PhD thesis, Université de Provence Aix-Marseille I.

Pirozzoli, S. & Bernardini, M. 2011 Turbulence in supersonic boundary layers at moderate Reynolds number. *Journal of Fluid Mechanics* **688**, 120–168.

Pirozzoli, S. & Grasso, F. 2006 Direct numerical simulation of impinging shock wave/turbulent boundary layer interaction at M=2.25. *Physics of Fluids* **18** (6), 065113.

Pirozzoli, S., Larsson, J., Nichols, J. W., Morgan, B. E. & Lele, S. K. 2010 Analysis of unsteady effects in shock/boundary layer interactions. In *Proceedings of the Summer Program 2010 at Center of Turbulence Research*.

Shahab, M. F. 2006 Numerical Investigation Of The Influence Of An Iminging Shock Wave And Heat Transfer On A Developing Turbulent Boundary Layer. PhD thesis.

Souverein, L. J. & Debiève, J.-F. 2010 Effect of air jet vortex generators on a shock wave boundary layer interaction. *Experiments in Fluids* **49** (5), 1053–1064.

Touber, E. & Sandham, N. D. 2009 Large-eddy simulation of low-frequency unsteadiness in a turbulent shock-induced separation bubble. *Theoretical and Computational Fluid Dynamics* **23** (2), 79–107.